

# UAV photogrammetry and structure from motion to assess calving- dynamics at Store Glacier, a large outlet draining the Greenland Ice Sheet

J. C. Ryan<sup>1</sup>, A. L. Hubbard<sup>2</sup>, J. E. Box<sup>3</sup>, J. Todd<sup>4</sup>, P. Christoffersen<sup>4</sup>, J. R. Carr<sup>1</sup>, T. O. Holt<sup>1</sup>  
and N. Snooke<sup>5</sup>

<sup>1</sup>Centre for Glaciology, Institute of Geography and Earth Sciences, Aberystwyth University, Aberystwyth, SY23 3DB, UK

<sup>2</sup>Department of Geology, University of Tromsø, N-9037 Tromsø, Norway

<sup>3</sup>Geological Survey of Denmark and Greenland, Copenhagen, Denmark

<sup>4</sup>Scott Polar Research Institute, University of Cambridge, Cambridge, UK

<sup>5</sup>Department of Computer Science, Aberystwyth University, Aberystwyth, SY23 3DB, UK

*Correspondence to:* Jonathan Ryan (jor44@aber.ac.uk)

*Technical correspondence to:* Neal Snooke (nns@aber.ac.uk)

## Abstract

This study presents the application of a cost-effective, unmanned aerial vehicle (UAV) to investigate calving dynamics at a major marine-terminating outlet glacier draining the western sector of the Greenland Ice Sheet. The UAV was flown over Store Glacier on three sorties during summer 2013 and acquired over 2,000 overlapping, geo-tagged images of the calving front at a ~ 40 cm ground sampling distance. Stereo-photogrammetry applied to these images enabled the extraction of high-resolution digital elevation models with vertical accuracies of  $\pm 1.9$  m which were used to quantify glaciological processes from early July to late August 2013. The central zone of the calving front advanced by ~ 500 m whilst the lateral margins remained stable. The orientation of crevasses and the surface velocity field derived from feature tracking indicate that lateral drag is the primary resistive force and that ice-flow varies across the calving front from  $2.5 \text{ m d}^{-1}$  at the margins to in excess of  $16 \text{ m d}^{-1}$

27 at the centreline. Ice flux through the calving front is  $3.8 \times 10^7 \text{ m}^3 \text{ d}^{-1}$ , equivalent to  $13.9 \text{ Gt a}^{-1}$   
28 <sup>1</sup> and comparable to flux-gate estimates of Store Glacier's annual discharge. Water-filled  
29 crevasses were present throughout the observation period but covered a limited area of  
30 between 0.025 - 0.24% of the terminus and did not appear to exert any significant control  
31 over fracture or calving. We conclude that the use of repeat UAV surveys coupled with the  
32 processing techniques outlined in this paper have great potential for elucidating the complex  
33 frontal-dynamics that characterise large calving outlet glaciers.

## 34 **1. Introduction**

35 Observational and modelling studies have demonstrated that Greenland's marine outlet  
36 glaciers have a complex and potentially non-linear response to both environmental forcing  
37 (e.g. Vieli et al., 2001; Benn et al., 2007; Holland et al., 2007; Howat et al., 2010; Hubbard,  
38 2011; Joughin et al., 2012; Walter et al., 2012; Carr et al., 2013) and to changes in front  
39 position (Howat et al., 2007, Luckman et al., 2006, Joughin et al., 2008). To quantify these  
40 processes and feedbacks, regular and accurate high-resolution measurements are required to  
41 capture the key spatio-temporal linkages between rates of ice calving, flow, surface lowering  
42 and frontal advance/retreat. Despite significant advances in satellite remote-sensing,  
43 limitations of spatial resolution (e.g. MODIS) and/or frequency of repeat imagery (e.g.  
44 Landsat or TerraSar-X (TSX)) renders detailed, day-to-day analysis of calving front  
45 dynamics unfeasible. On the other hand, acquisition of digital imagery from UAVs combined  
46 with the development of stereo-photogrammetry software has enabled the provision of high-  
47 resolution, 3D geo-referenced data on demand for geo-science applications (e.g. d'Oleire-  
48 Oltmanns et al., 2012; Hugenholtz et al., 2012, 2013; Whitehead et al., 2013; Lucieer et al.,  
49 2014). This represents an effective, cost effective technique for acquiring aerial data in  
50 remote, hazardous and/or inaccessible regions and recent applications for emerging snow and  
51 ice investigation abound the web (for example, see the highly informative site of Matt Nolan

52 (<http://www.drmattnolan.org/photography/2013/>). To date, published (peer-reviewed)  
53 application appears to be limited to the investigation of inter-annual changes of a land-  
54 terminating glacier on Bylot Island, Canadian Arctic (Whitehead et al., 2013).

55 Between July and August 2013, an off-the-shelf, fixed wing UAV equipped with a compact  
56 digital camera flew three sorties over the calving front of Store Glacier, West Greenland. The  
57 aerial photographs obtained during these flights were used to produce high-resolution (~ 40  
58 cm (Table 1)) digital elevation models (DEMs) and orthophotos of the glacier terminus.  
59 These data allowed the investigation of the spatially complex and time-varying glaciological  
60 processes operating at the glacier's calving front. The aim of this paper is to:

- 61 1) Detail the UAV, in terms of its payload and camera settings, and its specific  
62 deployment to Store Glacier.
- 63 2) Describe the techniques used for processing the aerial images and quantifying  
64 glaciological processes.
- 65 3) Discuss the significance of the data we obtained which includes calving events, the  
66 character, orientation and morphology of crevasses, surface velocities, ice discharge  
67 and changes in thickness and position of the calving front.

## 68 **2. Data and methods**

### 69 **2.1. Study site**

70 Store Glacier is a large marine-terminating (tidewater) outlet glacier located in the  
71 Uummannaq District of West Greenland (Fig. 1). The calving front has a width of 5.3 km and  
72 an aerial calving front (freeboard) of up to 110 m a.s.l. (Ahn and Box, 2010). Aerial  
73 photography from 1948 onwards reveals that Store Glacier's frontal position has remained  
74 stable over the last 65 years (Weidick, 1995). Seasonally, the calving front exhibits advance

75 and retreat of up to 400 m (Howat et al., 2010). The study here focuses specifically on glacier  
76 dynamics during the melt season under open-water, tidal modulation of ice flow.

## 77 **2.2.UAV platform**

78 The UAV airframe is an off-the-self 'Skywalker X8' ([www.hobbyking.com](http://www.hobbyking.com)) which has a  
79 wing-span of 2.12 m and is made from expanded polypropylene (EPP) foam (Fig. 2). For this  
80 deployment, the X8 was powered by two 5Ah 4-cell (14.8 V) Lithium Polymer batteries  
81 driving a 910 W brushless electric motor turning an 11 x 7 foldable propeller. In this  
82 configuration, the X8 has a flying mass of ~ 3 kg (including 1 kg payload), which allows a  
83 cruising speed of around 55 - 70 km per hour with a maximum range of ~ 60 km in benign  
84 conditions at constant altitude. A small propeller/high-revolution motor combination was  
85 chosen to provide maximum instantaneous thrust to ensure a clean launch (for novice  
86 operators) and to handle the potentially strong katabatic winds encountered during its 40 km  
87 sortie.

88 The autopilot is an open-source project called 'ArduPilot' (<http://ardupilot.com/>) based on a  
89 Atmel 2560 8bit microcontroller and standard radio control parts including 2.4 GHz radio  
90 control and pulse-width modulation (PWM) controlled servos for aileron and elevon control  
91 (Fig. 2). ArduPilot implements a dual-level proportional-integral-derivative (PID) controller  
92 architecture. The lower level controls flight stabilisation and the higher level controls based  
93 navigation. Tuning of the PID parameters is necessary to suit the mass and dynamics of the  
94 airframe to ensure accurate stabilisation without pitch/roll oscillation (lower-level controller)  
95 or flight path weaving (higher-level controller). The autopilot allows the UAV to fly  
96 autonomously according to a pre-programmed flight path defined by a series of 3D waypoints  
97 chosen by the user. The autopilot utilises a GPS for navigation, a triple axis accelerometer

98 and gyro for stabilisation, and a barometric pressure sensor for altitude control and these  
99 parameters are logged to memory at 10 Hz throughout the flight (Fig. 2).

100 The advantage of this package is that it can be assembled within a day from off-the-shelf  
101 parts and is cost-effective at less than US\$2,000. The X8 is also relatively straightforward to  
102 fly, robust, easily repairable and floats; all added bonuses when being deployed in remote  
103 areas by potential novices. Furthermore, the Ardupilot firmware is open source and hence can  
104 be programmed for specific requirements, for example camera triggering (see below).

105 Two lightweight digital cameras were tested at the field site: a Panasonic Lumix DMC-LX5  
106 10.1 megapixel (MP) camera with a 24 mm wide-angle zoom lens and a 16.1 MP Sony NEX-  
107 5N with a 16 mm fixed focal length lens though results presented here are limited to the  
108 former. A SPOT GPS tracking device was also included in the payload to facilitate recovery  
109 should a mission fail (which it did). The focal length of the Lumix lens was adjusted to 5.1  
110 mm (35 mm equivalent) to allow the widest possible coverage which gave the camera a 73.7°  
111 horizontal and 53.1° vertical field of view. A short exposure time of 1/1600 and a focal ratio  
112 of 8 were chosen to prevent overexposure and blurring of the ice surface. The Ardupilot  
113 open-source code was amended to trigger the camera automatically at user defined time or  
114 distance intervals at or between certain waypoints. The cameras were mounted pointing  
115 downwards within the airframe using neoprene and velcro straps to dampen vibration in a  
116 custom recessed aperture cut in the bottom with a UV filter to protect the lens and seal it.

### 117 **2.3.Flight planning**

118 The open-source software, APM Mission Planner (<http://plane.ardupilot.com/>) was used for  
119 flight waypoint manipulation and planning in conjunction with the 30 m Greenland Mapping  
120 Project (GIMP) DEM (Howat et al., 2014). To optimise spatial coverage against required  
121 resolution, flight endurance and stability, the UAV was programmed to fly at a constant

122 altitude of 500 m a.s.l. (Fig. 1). Based on the camera's focal length and field of view (53.1°  
123 by 73.7°) the ground (sea level) footprint at 500 m a.s.l. for each photo was ~450 x 750 m. To  
124 ensure coverage of the entire glacier terminus and overlap for successful photogrammetric  
125 processing, the four transects broadly parallel to the calving front were flown with ~250 m  
126 separation yielding a side overlap between photos of 70% (Fig. 1). The mean ground speed of  
127 the UAV was ~70 km h<sup>-1</sup> and camera trigger interval was adjusted between surveys. On  
128 flights 1 and 2, the interval between camera triggers was 1.5 s corresponding to a forward  
129 overlap of 94% and over 1000 geotagged images acquired. Flight 3 had a 2.4 s interval  
130 yielding a 90% forward overlap and 581 images (Table 1).

131 UAV operations were based out of a field camp with the advantage of a 50 m area of flat  
132 alluvial terrace with relatively boulder and bedrock free ground for manual remote control  
133 take off and landing. This location did, however, require a ~10 km transit to the calving front  
134 over a 450 m high peninsula which significantly reduced the useful endurance over the target.  
135 Of the six sorties flown over outlet glaciers in the region during July and August, 2013, the  
136 three over Store Glacier were most successful. Each sortie was 40 km long and ~35 minutes  
137 duration after the UAV had attained its operating altitude at the start of the mission and was  
138 passed from manual remote-control mode into autopilot mode (Fig. 1). Visual and remote-  
139 control contact is lost within a few km of the UAV being placed in autopilot mode hence  
140 validation of the mission plan is essential.

#### 141 **2.4. Three-dimensional model generation**

142 Three-dimensional data were extracted from the aerial photos using Agisoft Photoscan Pro  
143 software (Agisoft LLC, 2013). This software's strength lies in its ability to fully automate  
144 workflow and enables non-specialists to process aerial images and produce 3D models which  
145 can be exported as georeferenced orthophotos and DEMs (e.g. Fig. 3, 6). The first stage of

146 processing is image alignment using the structure-from-motion (SfM) technique. SfM allows  
147 the reconstruction of 3D geometry and camera position from a sequence of two-dimensional  
148 images captured from multiple viewpoints (Ullman, 1979). Photoscan implements SfM  
149 algorithms to monitor the movement of features through a sequence of multiple images and is  
150 used to estimate the location of high contrast features (e.g. edges), obtain the relative location  
151 of the acquisition positions and produce a sparse 3D point cloud of those features. The  
152 Ardupilot flight logs of the onboard navigation sensors allow the camera positions and the 3D  
153 point cloud to be georeferenced within instrument precision. SfM also enables the camera  
154 calibration parameters (e.g. focal length and distortion coefficients) to be automatically  
155 refined hence there is no need to pre-calibrate the cameras and lens optics (Verhoeven, 2011).

156 Once the photos have been aligned, a multiview reconstruction algorithm is applied to  
157 produce a 3D polygon mesh which operates on pixel values rather than features and enables  
158 the fine details of the 3D geometry to be constructed (Verhoeven, 2011). The user determines  
159 the precision of the final 3D model based on image resolution and pixel footprint. A medium  
160 quality setting was chosen yielding DEMs with between 38 – 40 cm/pixel ground sampling  
161 resolution (GSD), which were resampled to a Cartesian 50 cm grid to enable intercomparison  
162 (Table 1). Higher resolutions (<30 cm GSD) are attainable but the increase in computational  
163 time and the accuracy of georeferencing limits the benefits of such apparent precision.

164 Two problems of accuracy were encountered in DEM production: 1) Photoscan failed to  
165 reconstruct a flat sea level of constant elevation, and, 2) that relative positional errors  
166 between the DEMs constructed from different sorties were up to 17.12 m horizontally and  
167 11.38 m vertically. Positional errors were due to the specified limits of the onboard L1 GPS  
168 of  $\pm 5.0$  metres horizontally and, when combined with the barometric sensor, to a similar  
169 accuracy vertically. These were compounded by the time lag between the camera triggering

170 and actual photograph acquisition. Hence, a secondary stage of processing was carried out  
171 which involved 3D co-registration of the DEMs. To do this, the horizontal and vertical  
172 coordinates of common control points (CPs) based on distinct features such as cliff bases,  
173 large boulders and promontories were extracted from the georeferenced orthoimages. The  
174 CPs that were at sea level were nominally given elevation values of zero, re-imported into  
175 Photoscan and subsequently reprocessed along with a geodetic GPS ground CP located at  
176 70.401°N, -50.665°E and 335.85 m altitude on the bedrock headland overlooking the  
177 glacier's northern flank. During this secondary stage of processing, Photoscan's optimization  
178 procedure was run to correct for possible distortions. After processing with the CPs, a flat sea  
179 level across the glacier front was produced and the relative errors between the three DEMs  
180 were reduced to  $\pm 1.41$  m horizontally and  $\pm 1.90$  m vertically. The georeferenced 3D DEMs  
181 and orthophotos were then exported at 50 cm pixel size for further analysis in ArcGIS and  
182 ENVI software packages.

### 183 **2.5. Analysis**

184 Changes in calving front positions were obtained from these data combined with a Landsat 8  
185 panchromatic image obtained on 12 June (Fig. 3B). Each calving front position was digitized  
186 according to the procedure outlined by Moon and Joughin (2008) whereby a polygon of the  
187 calving front retreat or advance is digitized and divided by the width of the glacier. This  
188 method has been used in previous studies (e.g. Howat et al., 2010; Schild and Hamilton,  
189 2013) and enables intercomparison of results. Surface elevation change was calculated from  
190 the residual difference of the DEMs (Fig. 3A).

191 Ice flow across the terminus region was calculated by feature tracking performed on  
192 successive DEMs using the ENVI Cosi-CORR software module (Fig. 4B). These velocities  
193 were then used to estimate ice flux through the calving front for the same period under the



194 assumption of plug flow (uniform velocity profile with depth) and using an calving front  
195 cross-section obtained from Xu et al. (2013) and modified by single and multi-beam echo  
196 sounder bathymetry obtained by S/V Gambo in 2010 and 2012 (Chauché, unpublished). The  
197 frontal cross-section was divided into 10 m vertical strips and. and under the plug-flow  
198 assumption, each was assigned its corresponding horizontal velocity (Fig. 4A). The floatation  
199 depth and buoyancy ratio across the calving front was calculated using the ice surface  
200 (freeboard) elevation and total ice thickness with a value for the density of ice of  $917 \text{ kg m}^{-3}$   
201 for sea water of  $1028 \text{ kg m}^{-3}$  (Fig. 5A).

202 To investigate the distribution and patterns of crevassing, each DEM was Gaussian filtered at  
203 200 pixels (100 m) in ArcGIS and subtracted from the original DEM to yield the pattern of  
204 negative surface anomalies. These anomalies were converted into polygons to map and hence  
205 quantify crevasse distribution and character (Fig. 6A). The resulting polygons were enclosed  
206 by a minimum bounding rectangle, which allowed the orientation, width, length and depth of  
207 crevasses to be extracted (Fig. 6A, Table 2). Water-filled crevasses were automatically  
208 located in the ENVI package using the supervised maximum likelihood classification (MLC)  
209 method. Representative training samples for water-filled areas were chosen from the colour  
210 composite orthophoto (Fig. 6B). The trained tool then classifies pixels that are interpreted as  
211 water into the desired class. The resulting raster image was converted into a shapefile and  
212 used to mask and define the area of the water-filled crevasses across the terminus. These  
213 procedures allow thousands of crevasses in multiple orthoimages and DEMs to be quantified  
214 easily without the difficulties and dangers associated with direct field measurements.

## 215 **2.6.Uncertainties and limitations**

216 The relative horizontal uncertainties between the DEMs were investigated by feature tracking  
217 the stationary bedrock at the sides of the glacier. The RMS horizontal displacement was  $\pm$

218 1.41 m which provides us with an approximate error estimate. The relative vertical  
219 uncertainties between the DEMs were estimated by calculating elevation differences between  
220 bedrock areas, which reveal an error estimate was  $\pm 1.9$  m. The two-stage procedure outlined  
221 in Section 2.4 therefore enabled us to improve the relative positional uncertainties from  
222 nearly 20 m to less than 2 m. For future studies, it is thought that several CPs on the bedrock  
223 either side of the glacier front would further reduce these uncertainties. A telemetric  
224 differential GPS deployed on or near the calving front, which is sufficiently large/bright to  
225 identify within the aerial imagery would allow further ground control in the centre of DEMs,  
226 away from bedrock CPs.

227 Due to the lack of reflected light from deep crevasse recesses, the DEM generation process  
228 cannot quantify the narrowest sections of all fractures and resultant crevasse depths are  
229 therefore a minimum estimate. The technique is also clearly limited to line of sight  
230 precluding narrow fractures which extend for tens of centimetres horizontally and potentially  
231 up to a few metres vertically (Hambrey and Lawson, 2000; Mottram and Benn, 2009).

232 Finally, there are a number of practical difficulties when operating an autonomous aircraft in  
233 remote and inaccessible environments. Mission planning is critical; knowledge of the local  
234 weather conditions, as well as up-to-date satellite imagery and DEMs are a prerequisite.

### 235 **3. Results**

236 Three successful UAV sorties were flown over Store Glacier calving front providing  
237 imagery, orthophotos and DEMs on 1 and 2 July and the 23 August, herein referred to flights  
238 and associated products 1 to 3, respectively (Table 1). The interval between flights 1 and 2  
239 was 19 hours and comparison between these outputs enables identification of processes  
240 operating over a daily (short) timescale, be it a very specific snapshot. The third sortie was  
241 flown 52 days later and comparison between these outputs enables investigation of late-

242 seasonal change. The footprint of the four cross-glacier transects flown extend just over 1 km  
243 up-stream from the calving front and herein, this section is referred to as ‘the terminus’.

### 244 **3.1.Short timescale calving and surface elevation change**

245 Residual elevation change between 1 and 2 July (Fig. 3A) reveals that the front retreated in  
246 two sections by up to 50 and 80 m respectively. The more northerly calving event (A)  
247 resulted in a 450 m wide section of the terminus retreating by between 20 and 50 m, whilst  
248 event B produced between 20 m and 80 m of retreat across a 400 m section (Fig. 3A). In  
249 addition to these two calving events (which are discussed in section 3.6), the central 4.5 km  
250 frontal section advanced between 12 m to 16 m (Fig. 3A). At its lateral margins, the calving  
251 front shows no discernible systematic change though there are isolated, small calving events,  
252 for example, within 50 m of the southern flank (Fig. 3A). Upstream of the calving front, there  
253 is no net change in mean surface elevation away from the front and the dappled pattern of  
254 residual elevation change is a result of the advection of crevasses and seracs. Successive long  
255 profiles of the terminus between the 1 and 2 July reveal specific down-glacier crevasse  
256 advection with flow (Fig. 6) at a rate of 5 and 16 m d<sup>-1</sup> on Profile 1 and 2, respectively. These  
257 results provide corroboration for the surface velocities derived by feature tracking in Section  
258 3.4.

### 259 **3.2.Seasonal timescale calving front position and surface elevation change**

260 Over the entire melt season, larger fluctuations in calving front position are observed (Fig.  
261 3B). Over the 19 day period from 12 June to 1 July, mean frontal retreat was 160 m (Fig. 3C)  
262 and between 2 July and 23 August, the calving front advanced by an average of ~110 m to a  
263 position similar to that in 12 June (Fig. 3D). These mean values, however, do not convey the  
264 full extent and detail of the changes observed in the calving front. For example, the central  
265 section of the calving front retreated by up to 525 m between the 12 June and 1 July and

266 advanced by up to 450 m between 2 July and 23 August (Fig. 3B). Furthermore, the lateral  
267 margins of Store Glacier (the southern 850 m and the northern 1.5 km) are relatively stable  
268 with  $< 50$  m change in position. Over the 52 day period between 2 July (Flight 2) and 23  
269 August (Flight 3) widespread surface lowering of 6.1 m (or  $0.12 \text{ m d}^{-1}$ ) was observed across  
270 Store Glacier terminus (Fig. 4A), which is significantly larger than the estimated vertical  
271 uncertainties of the DEMs ( $\pm 1.9$  m). Despite the same dappled patterns caused by local  
272 advection of crevasses and seracs, we infer this to be associated with dynamic thinning 1 km  
273 upstream of the calving front, which is discussed in Section 4.2.

### 274 **3.3.Bathymetry**

275 The deepest sector of the calving front is located 1 km south of the centreline and exceeds  
276 540 m below sea level (Fig. 5A). This 200 m wide sector also corresponds to the greatest  
277 thickness of  $\sim 600$ m. To the south of this deepest point, the bottom rises rapidly to a 200 m  
278 deep shelf located 500 m from the flank. To the north of the deepest point, the bottom  
279 shallows more gently to within 400 m where it becomes steeper towards the fjord wall.

### 280 **3.4.Surface velocities**

281 Maximum surface flow velocities of  $16 \text{ m d}^{-1}$  between 1 and 2 July are consistent with results  
282 obtained in previous studies using other techniques, such as feature tracking images from a  
283 land-based time-lapse camera (between  $11$  and  $15 \text{ m d}^{-1}$ ) (Ahn and Box, 2010; Walter et al.,  
284 2012). The spatial pattern of surface flow from feature tracking of images between the 1 and  
285 2 July varies considerably across the terminus of Store Glacier (Fig. 4B) attaining velocities  
286 of  $16 \text{ m d}^{-1}$  ( $5.8 \text{ km a}^{-1}$ ) near the centre of the glacier down to  $2.5 \text{ m d}^{-1}$  at the lateral flanks.  
287 Surface velocities are related to slope, depth, thickness and distance from the lateral margins  
288 (Fig. 5C, D). As would be expected, maximum velocities correlate with maximum depth and  
289 towards the north flank are linearly correlated ( $R^2 = 0.90$ ) with frontal depth (Fig. 5C).

290 Towards the southern flank the relationship is less apparent especially between 200 to 350 m  
291 depths. There is a strong correlation between velocities and distance from the lateral margins  
292 which can be approximated by a power function ( $R^2 = 0.90$ ) (Fig. 5D). Although application  
293 of the floatation criteria reveal parts of calving front to be buoyant (Fig. 5A), side-scan sonar  
294 observations reveal that the glacier toe was resting fjord bed (Chauché, unpublished). When  
295 the surface flow pattern is combined with frontal bathymetric data we estimated that the mass  
296 flux through the calving front of Store Glacier was  $3.8 \times 10^7 \text{ m}^3 \text{ d}^{-1}$ , equivalent to  $\sim 13.9 \text{ Gt a}^{-1}$ .  
297 <sup>1</sup>.

298 Seasonal flow patterns were not obtainable between 2 July and 23 August as the majority of  
299 any matching features within the study area required for tracking had already calved into the  
300 ocean. Furthermore, it is likely that the morphology of many crevasses and seracs will have  
301 changed significantly through melt and deformation and would not be recognised by the  
302 cross-correlation procedure.

### 303 **3.5.Crevassing**

304 The morphology and orientation of crevasses varies markedly across the terminus (Fig. 6).  
305 The largest crevasses occur in a sector south of the glacier centre line in zone 4 (Fig. 6, Table  
306 2). Here, crevasses have mean minimum depths of 18 m, lengths of 68 m and widths of 31 m.  
307 The largest crevasses are up to 30 m deep, over 500 m long and nearly 200 m wide but no  
308 crevasses that penetrated below sea level were identified. Most crevasses in this region are  
309 arcuate with limbs pointing towards the calving front and are orientated obliquely to the  
310 direction of ice flow (Fig. 6). This arcuate morphology of crevasses continues across the  
311 central 3 km of the terminus in zone 3 (Fig. 6). Here, crevasses have mean a depth of 10.5 m,  
312 length of 50 m and widths of 18 m (Table 2). In zone, 2, 300 to 500 m from the northern  
313 flank, crevasses are aligned obliquely to the direction of ice flow ( $30 - 45^\circ$ ). Up to the fjord

314 walls in zones 1 and 5, crevasses are generally orientated parallel to the ice flow ( $> 15^\circ$ ) (Fig.  
315 6, Table 2) and are much smaller with a mean lengths of 22 m and width of 8 m (Table 2). No  
316 discernible difference in average crevasse depths, lengths or widths was observed between  
317 the early July and late August and the pattern and character of crevassing was also similar.

318 Water-filled crevasses were clustered in zone 4, coinciding with the sector of larger crevasses  
319 (Fig. 6B). Water-filled crevasses covered 12,000 m<sup>2</sup> or 0.24 % of the survey area (to ~ 1 km  
320 from the calving front) on 2 July (Table 1). Some 42 individual water-filled crevasses were  
321 identified with the largest having an area of 1,200 m<sup>2</sup>. By 23 August, the number, size and  
322 total area of water filled crevasses were lower: only 10 water-filled crevasses could be  
323 identified, the largest of which was 400 m<sup>2</sup> and with a total area of 1,230 m<sup>2</sup> (0.025% of the  
324 survey area). We were not able to ascertain the depth of water in the crevasses as no common  
325 crevasses could be identified which drained or filled between flights but this would be a  
326 specific aim of future studies which, with regular sorties, could potentially determine the  
327 depth of a crevasse before filling or after drainage or otherwise exploit the light reflectance  
328 relationship with water depth (e.g. Fitzpatrick et al., 2014).

329 Successive profiles of the terminus from 1 and 2 July demonstrate how the UAV surveys are  
330 capable of capturing the displacement of crevasses, which advect downstream at a rate of 5  
331 and 16 m d<sup>-1</sup> in Profiles 1 and 2, respectively (Fig. 6). The techniques used in this study are  
332 therefore capable of identifying changes in crevasses geometry, particularly width and depth  
333 through time.

### 334 **3.6. Calving events**

335 The two calving events identified between 1 and 2 July appear to take place under contrasting  
336 conditions. Event A consisted of the calving of multiple, relatively small ice blocks with the  
337 glacier failing along two main crevasses located 30 and 50 m behind the calving front. These

338 crevasses were between 8 and 10 m deep, respectively and in this instance, the crevasses  
339 located closest to the front were the ones that failed. Event B appears to be a single large  
340 event caused by the fracturing of a series of parallel crevasses which were up to 14 m deep  
341 and 60 m behind the calving front. Unlike, calving event A, the crevasses that failed in event  
342 B were not the closest to the calving front. Indeed, there were other crevasses that were  
343 deeper and located nearer to the front, yet did not calve. Water was not observed in any of the  
344 crevasses along which calving took place.

## 345 **4. Discussion**

### 346 **4.1.Changes occurring over a daily timescale**

347 The orientation of crevasses suggests that lateral drag is an important resistive stress on Store  
348 Glacier. The lateral margins of the Store are characterised by crevasses that are orientated  
349 parallel to the direction of flow which suggests that they have formed in response to simple  
350 shear stresses associated with the drag of the fjord walls (Fig. 6) (Benn and Evans, 2010).  
351 The importance of lateral drag is further demonstrated by the morphology of crevasses found  
352 near the glacier flowline (Fig. 6). Their arcuate nature indicates that the principal tensile  
353 stresses operating on the ice have been rotated by lateral gradients in ice velocity. These  
354 gradients are caused by the simple shear stress between the fjord walls and the margins of the  
355 glacier which cause the ice to flow slower (Fig. 4B) (Benn and Evans, 2010).

356 The simple shearing caused by velocity gradients is further demonstrated by the differing  
357 relationship between velocity and depths between the north and south side of the glacier (Fig.  
358 5C, D). On the north side, the velocity increases gradually from the fjord wall to the centre of  
359 the glacier, reflecting the gradual deepening of bathymetry and the resulting decrease of basal  
360 and lateral drag. On the south side, the velocities are higher than the north side for given  
361 depths and distances from the lateral margins (Fig. 5C, D). We hypothesize that, because the

362 deepest part of the glacier is situated 1 km south of the centreline, the ice on south side is  
363 more influenced by faster flowing ice which exerts a simple shear stress on the shallower,  
364 adjacent ice (250 – 400 m thick). This causes the shallow ice to flow faster than ice with  
365 similar thicknesses and distance from the lateral margins on the north side (Fig. 5C).

366 The mass flux through the calving front was calculated at  $3.8 \times 10^7 \text{ m}^3 \text{ d}^{-1}$  which needs to be  
367 balanced by three main frontal processes: calving, submarine melting and advective advance.  
368 Both calving and advance were observed in this study but it is likely that submarine melting  
369 also has a large role in ice output at a daily timescale. For example, Xu et al. (2013) used  
370 oceanographic data to calculate a melt water flux of between 0.5 and  $1.1 \times 10^7 \text{ m}^3 \text{ d}^{-1}$  from  
371 Store Glacier in August, 2010 equivalent to 13 - 29% of the mass flux calculated in by our  
372 study. For comparison, Rink glacier has an ice flux of  $3.0 \times 10^7 \text{ m}^3 \text{ d}^{-1}$  of which 27% is  
373 estimated to be lost through submarine melting each day (Enderlin and Howat, 2013).

#### 374 **4.2. Changes occurring over a seasonal timescale**

375 The lack of variation in the position of the lateral margins of the glacier shows that a balance  
376 is maintained between the ice flux input and submarine melting and calving output in this  
377 zone throughout the melt season. The balance could be explained by the mechanism of  
378 calving events. At the lateral margins calving is characterised by small, regular events such as  
379 calving event A (Fig. 3A). The regularity of these small events means that any small advance  
380 or retreat is regulated almost instantly by changes in calving rate which returns the lateral  
381 margins of the glacier to the same position. Calving rate could also be moderated by changes  
382 in the bathymetry. When the lateral margins advance, calving rates increase due to the abrupt  
383 deepening of the bathymetry seaward of the lateral margins of the glacier which cause basal  
384 drag to be reduced. Ice flow acceleration can lead to increased longitudinal stretching and



385 deeper crevassing, thereby increasing calving rate and leading to retreat to its original,  
386 bathymetrically-pinned position.

387 The centre of the calving front is much more active with calving and submarine melt rates  
388 that vary on a seasonal timescale. We propose that the main cause of variability is due to  
389 calving rates which are highly irregular throughout the melt season (Jung et al., 2010). Our  
390 observations also support the suggestion that calving rates are dominated by major calving  
391 events which have a time interval of around 28 days (e.g. Jung et al., 2010). If the calving  
392 front advances for 28 days at  $16 \text{ m d}^{-1}$ , it will advance  $\sim 448 \text{ m}$ . A large, single calving event  
393 can therefore yield a retreat of  $\sim 448 \text{ m}$  and would explain the variation in the position of the  
394 calving front during the melt season (Fig. 3B). On 25 August 2013, a tabular iceberg with a  
395 length of  $\sim 500 \text{ m}$  was observed to calve from the central zone of Store Glacier.

396 Towards the end of the melt season (23 August), a widespread surface deflation of  $0.12 \text{ m d}^{-1}$   
397 was observed (Fig. 4A). Application of a simple degree-day model reveals that part of this  
398 lowering can be attributed to ablation. Average daily air temperatures were recorded at an  
399 automated weather station (AWS) located near the UAV launch site (Fig. 1) and, using a  
400 melt-factor of  $6 - 10 \text{ mm per degree per day}$  (Hock et al. 2005), surface lowering due to  
401 ablation is estimated between  $0.038 - 0.064 \text{ m d}^{-1}$ . It follows that ablation alone cannot  
402 account for the entire lowering rate observed and, hence, we infer an additional component of  
403 dynamic thinning due to relative strain-extension across this zone, related to reduced up-  
404 stream delivery of flux and/or frontal kinematics associated with enhanced late-season  
405 submarine melting and/or calving rates. GPS measurements by Ahlstrom et al. (2013)  
406 tentatively support the former interpretation and reveal that surface velocities 8 km upstream  
407 of Store's calving front tend to decrease between July and August. However, this raises  
408 questions regarding the timescales over which dynamic thinning and surface melt occur and  
409 whether or not the flow regime across the terminus is, to some extent, isolated or operating

410 independent from processes upstream supplying mass. Either way, these questions are  
411 beyond the scope of the datasets presented here and require a study of greater areal extent and  
412 temporal coverage.

413 Another important observation is the order of magnitude reduction of the area of water-filled  
414 crevasses between early July and late August (Fig. 6). Surface air temperatures directly  
415 influence the extent of water-filled crevasses. AWS data reveal that mean daily air  
416 temperature was  $\sim 6^{\circ}\text{C}$  during the four days prior to the UAV sortie on the 2 July. In contrast,  
417 mean temperature was  $\sim 3.5^{\circ}\text{C}$  on the four days prior to the UAV sortie on 23 August. Water-  
418 filled crevasses have been hypothesized to penetrate deeper than crevasses without water  
419 (Weertman, 1973; Van der Veen, 1998) and hence act as mechanism for calving (Benn et al.,  
420 2007). The calving events observed in this study did not specifically fail at water-filled  
421 crevasses and hence our limited results show no support for this mechanism. However,  
422 studies of greater scope with daily coverage will be required to determine definitively if  
423 water-filled crevasses have any appreciable impact on calving dynamics at Store Glacier or  
424 elsewhere.

## 425 **5. Conclusions and future directions**

426 A UAV equipped with a commercial digital camera enabled us to obtain high resolution  
427 DEMs and orthophotos of the calving front of a major tidewater glacier at an affordable price.  
428 Airborne Lidar currently presents the only alternative method for acquiring DEMs with  
429 comparable accuracy and precision. However, to fly consecutive sorties in a remote  
430 environment is likely to be prohibitively expensive and with sufficient ground control points  
431 the digital photogrammetry approach may also exceed the accuracy of this technique.

432 The three sorties flown enabled key glaciological parameters to be quantified at sufficient  
433 detail to reveal that the terminus of Store Glacier is a complex system with large variations in

434 crevasse patterns surface velocities, calving processes, surface elevations and front positions  
435 at a daily and seasonal timescale. Surface velocities vary across the terminus and are  
436 influenced by both basal and lateral drag (Fig. 4B, 5C, D). The oblique orientation and  
437 arcuate nature of crevasses suggests that the principal extending strain rate is orientated  
438 obliquely to the direction of flow and we therefore propose that resistive stresses at the  
439 terminus of Store Glacier are dominated by lateral drag (Fig. 6). With this in mind, the retreat  
440 of Store into a wider trough could significantly increase the ice discharge. We estimated that  
441 the ice flux through the calving front of Store was  $13.9 \text{ Gt a}^{-1}$  and we observed a small  
442 terminus advance between 1 and 2 July (Fig. 3A, 5A). This advance reveals that, during this  
443 period, the sum of calving and submarine melt rates are less than the ice flux. Calving is an  
444 irregular process and that the position of the calving front returned to its 12 June position by  
445 23 August suggests that over this timescale calving and submarine melting balance ice flux  
446 (Fig. 3B). Water-filled crevasses covered 0.24% of the survey area on 2 July but this fell to  
447 0.025% on 23 August (Fig. 6). It remains to be seen whether water-filled crevasses are more  
448 likely to initiate calving events but our tentative results here indicate no support this  
449 mechanism.

450 Future studies, with more frequent sorties could be used to compare and investigate further  
451 glaciological changes over a more continuous timespan. There is also the possibility of more  
452 sophisticated payloads with radiation, albedo and other multi-band sensors as well as radar  
453 and laser altimetry. There are many potential cryospheric applications for investigation such  
454 as sea ice, marine and terrestrial-terminating glaciers and, with increased range, ice sheets,  
455 that can be achieved with the use of repeat UAV surveys. We have demonstrated that for  
456 calving outlet glaciers, a UAV carrying a high resolution digital camera would be sufficient  
457 to investigate the following projects:

- 458 • Analysis of the thickness and back-stress exerted by the ice mélange during the winter  
459 and the effect of its break out on glacier flow, calving rate and character.
- 460 • Seasonal changes in the depth, density, orientation and nature of crevassing and their  
461 impact on calving rate and character.
- 462 • The influence of daily to seasonal melt and supraglacial lake drainage on downstream  
463 dynamics and calving.
- 464 • Analysis of daily to seasonal fluctuations in calving flux, terminus position and  
465 impact on upstream dynamics and thinning.

466

467

468

469

470

471

472

473

474

475

476

477

478

479 **Tables**

480 **Table 1.** Attributes of the flight surveys and image acquisition of the UAV

Flight no.	Date	Interval between pictures (s)	No. images	Glacier coverage (km <sup>2</sup> )	Resolution of DEM (cm/pixel)
1	01 July	1.55	611	3.17	40
2	02 July	1.51	1051	4.95	38
3	23 August	2.36	567	5.02	39

481

482 **Table 2.** Attributes of mean crevasse width, length and orientation in each zone labelled in  
483 Figure 5. Orientations are measured along the long-axis of each crevasse and are in respect to  
484 the direction of flow which is 0°.

Zone	Mean width (m)	Mean length (m)	Mean orientation (°)
Zone 1	3.6	9.4	9.2
Zone 2	4.8	14.0	36.7
Zone 3	10.5	32.6	85.1
Zone 4	6.5	17.8	60.4
Zone 5	3.5	8.5	10.8

485

486

487

488

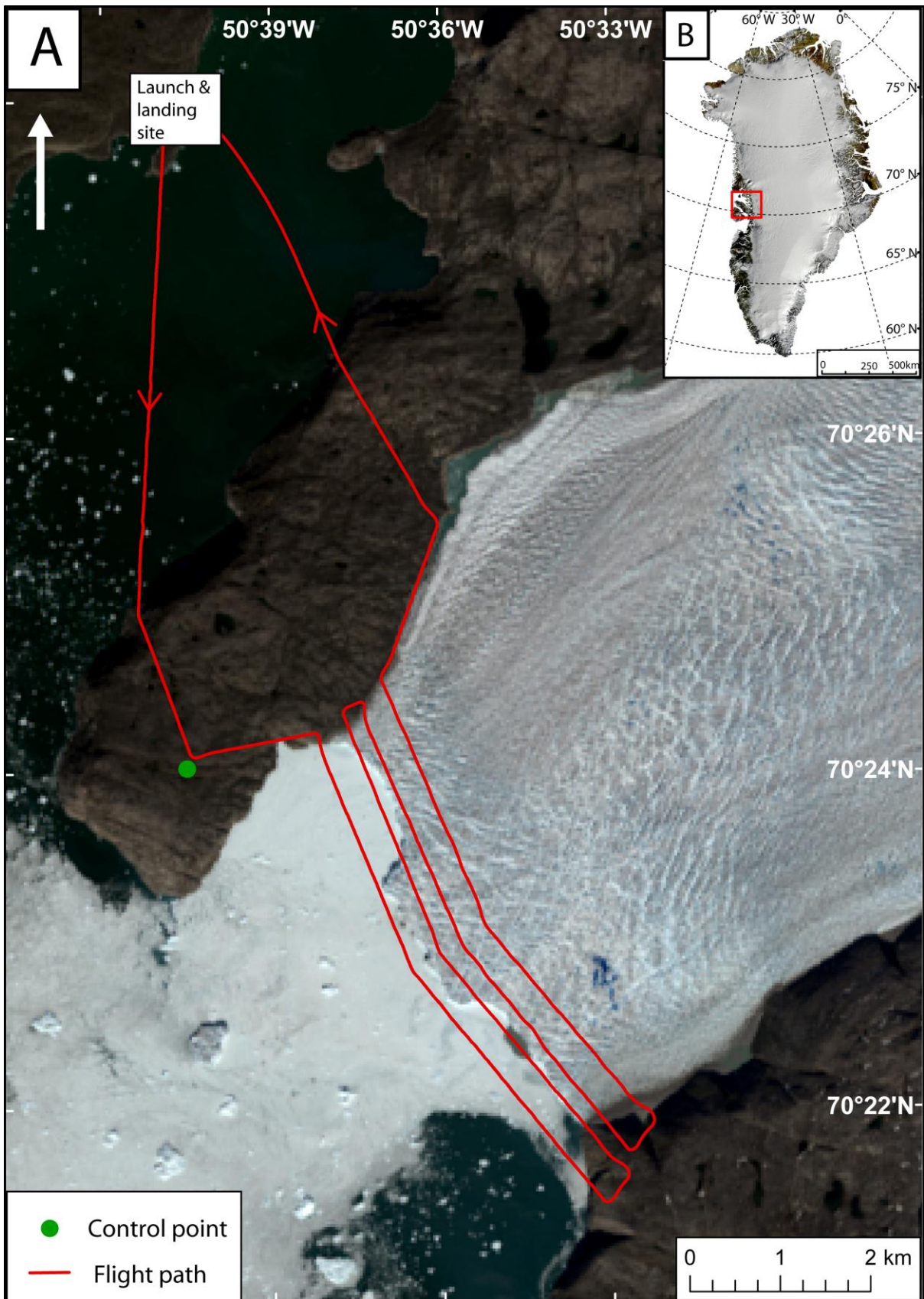
489

490

491

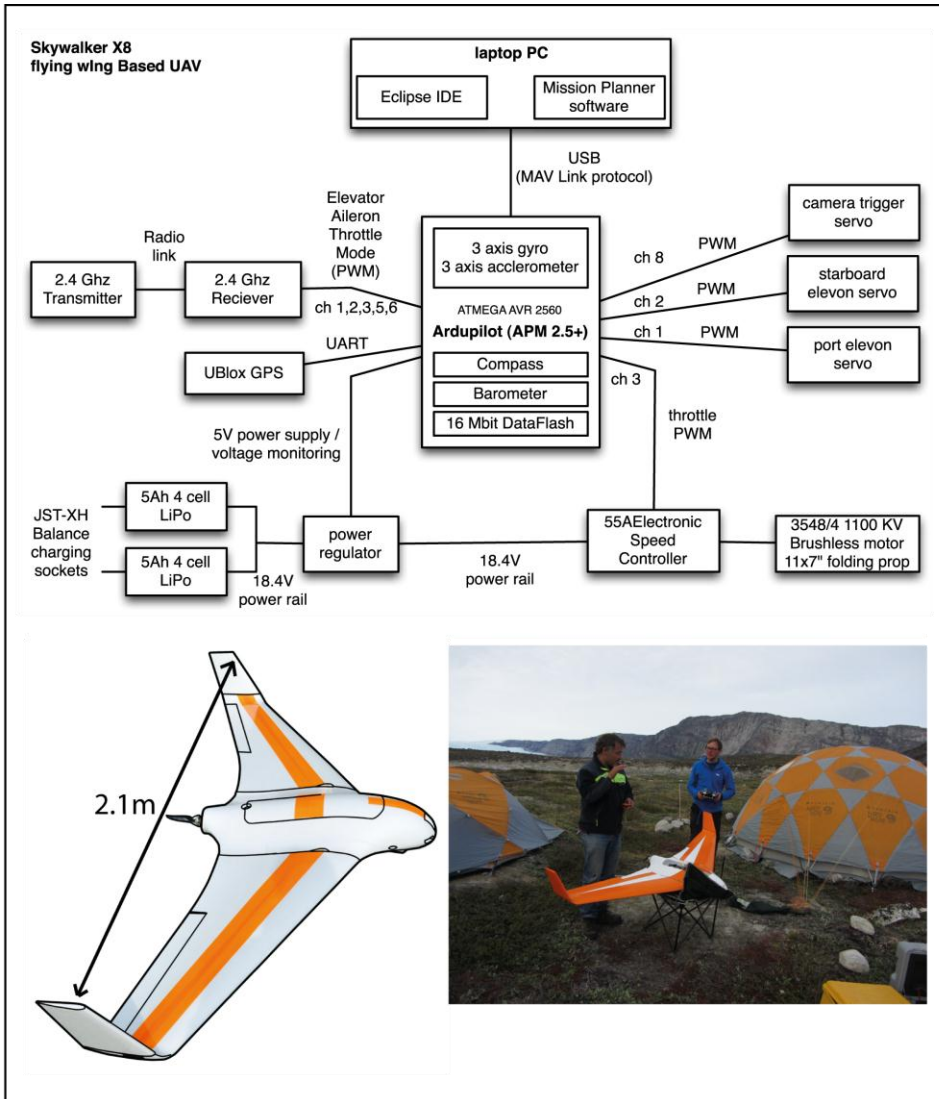
492

493 **Figures**



494

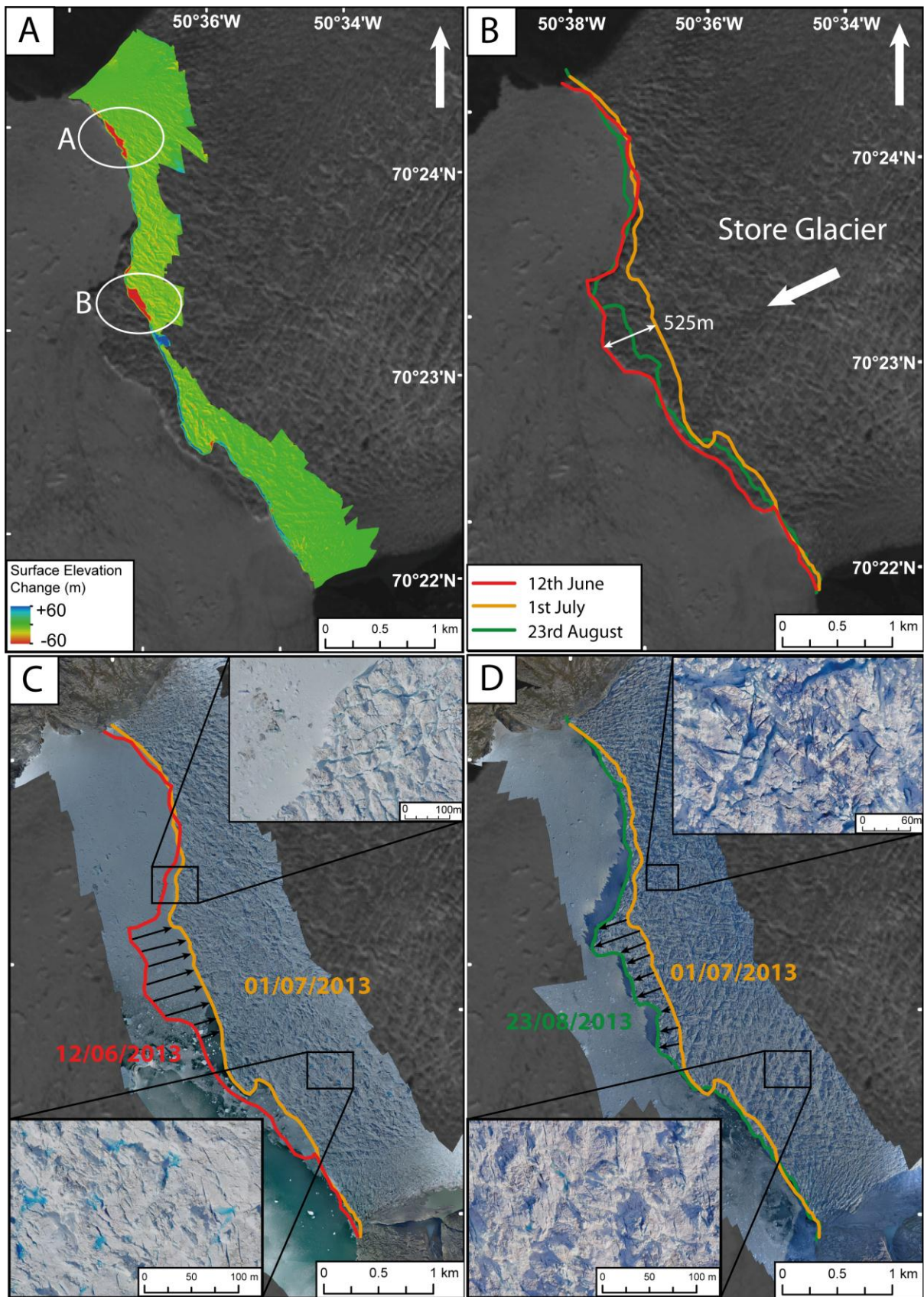
495 **Figure 1.** (A) A typical UAV sortie over Store Glacier. The background map is a Landsat 8  
 496 true colour image from 12 June 2013. The red line shows the UAV flight path on the 2<sup>nd</sup> July  
 497 2013. (B) Location of Store Glacier in the Uummannaq Region, West Greenland on a  
 498 MODIS mosaic image of Greenland (Kargel et al., 2012).



499  
 500 **Figure 2.** Flowchart of the control set up and picture of the UAV at base camp with the  
 501 ‘relative novices’.

502

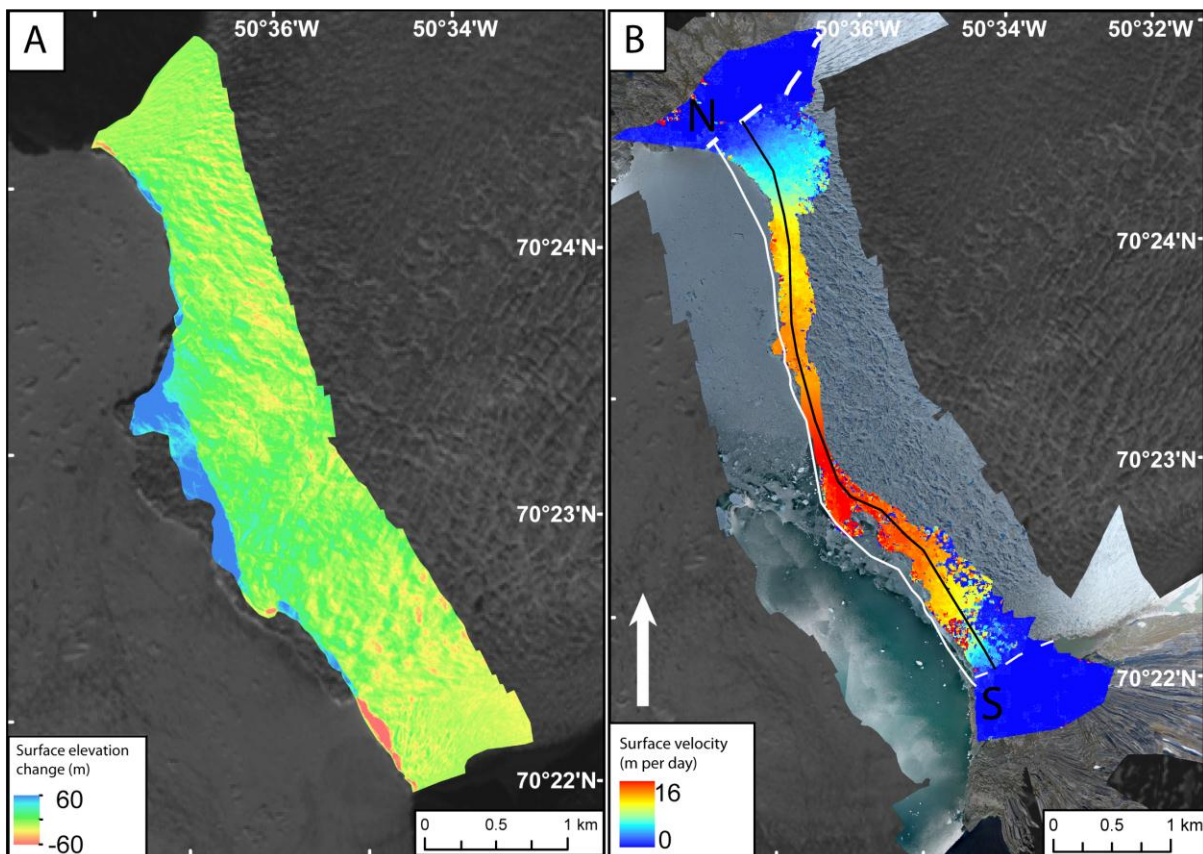




503

504 **Figure 3.** (A) Surface elevation difference between two DEMs collected on 1 July and 2 July.  
 505 Red areas show elevation loss whilst blue areas show elevation gain. White circles highlight  
 506 the calving events that occurred between the two UAV surveys. (B) The position of the  
 507 calving front of Store Glacier during the summer of 2013. (C) Calving front retreat observed  
 508 between 12 June and 1 July. Inset is an orthorectified image of the water-filled crevasses  
 509 observed on 1 July with a pixel resolution of 30 cm. (D) Calving front advance observed  
 510 between 1 July and 23 August. Inset is an orthorectified image showing water-filled crevasses  
 511 observed on 23 August. The coverage and size of water-filled crevasses is smaller.

512

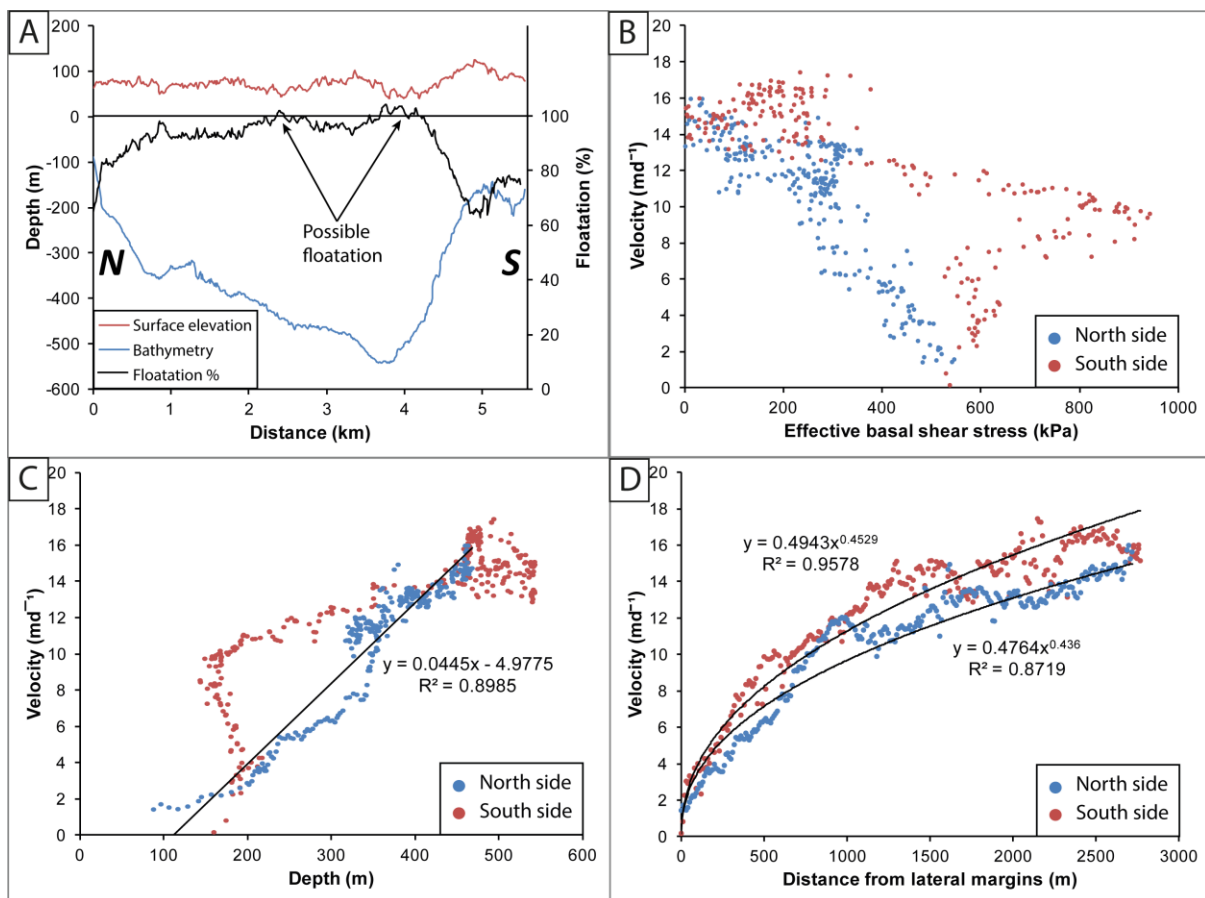


513

514 **Figure 4.** (A) Surface elevation changes between 2 July and 23 August. An average thinning  
 515 of  $0.12 \text{ m d}^{-1}$  was estimated for the surveyed area. (B) The ice flow speed structure of the  
 516 terminus of Store Glacier between 1 and 2 July 2013. The centre of the glacier flows at

517 approximately  $16 \text{ m d}^{-1}$  whilst the margins flow less than  $5 \text{ m d}^{-1}$ . Dotted white lines show the  
 518 lateral margins of the glacier. The black line represents the locations of the horizontal  
 519 velocity and surface elevation values that were used to estimate ice flux. The white line  
 520 represents the location of the depth values used to estimate ice flux. The cross-section of the  
 521 calving front derived from these profiles is displayed in Fig. 4A.

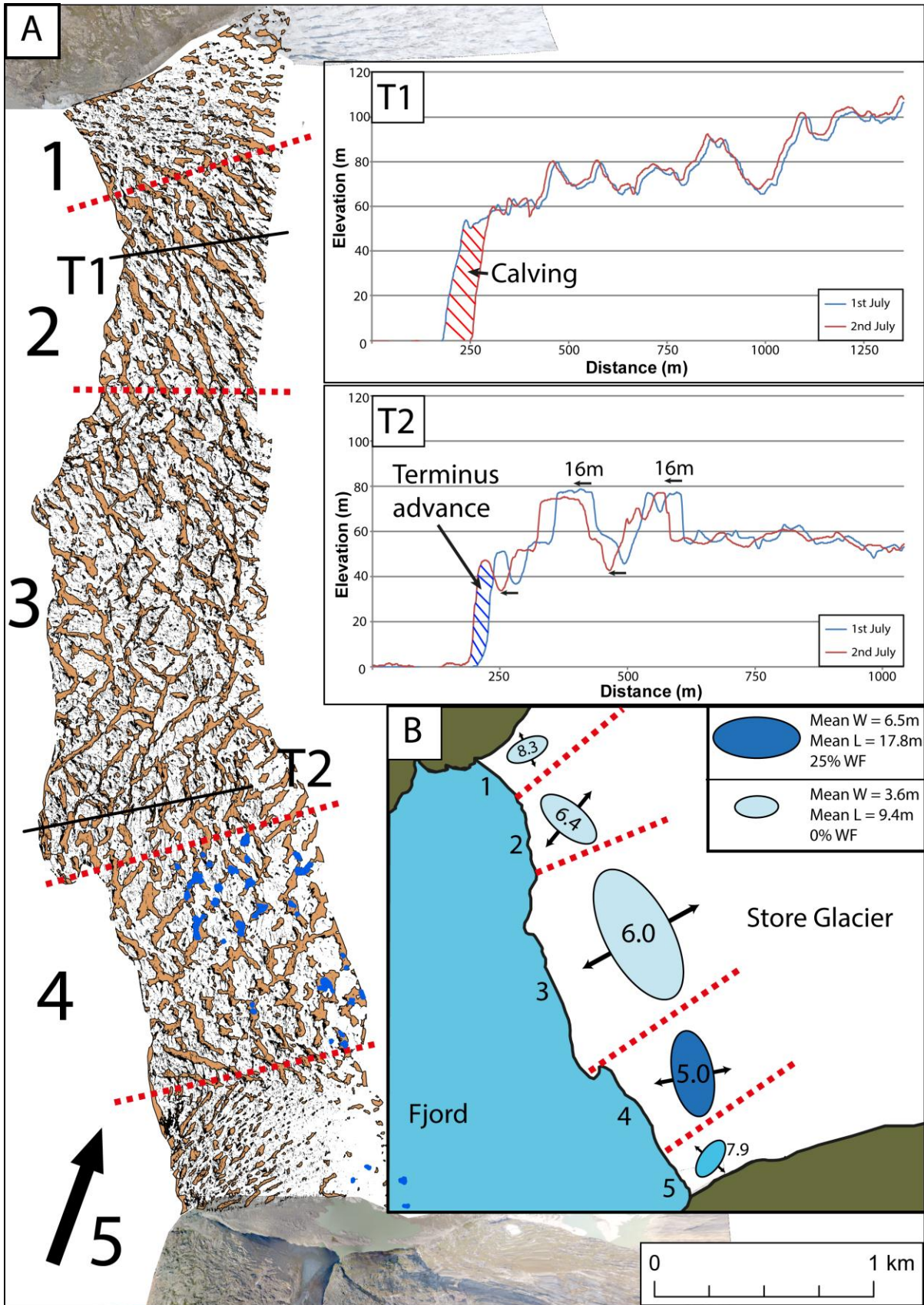
522



523

524 **Figure 5.** (A) Profiles showing the sea floor bathymetry and ice surface elevation at the  
 525 calving front. These data were combined with surface velocities to estimate the ice flux of  
 526 Store Glacier. Where the floatation percentage is over 100%, it is assumed that the ice is not  
 527 thick enough to be fully grounded in hydrostatic equilibrium. (B) The relationship between  
 528 effective basal shear stress and velocity. (C) The relationship between depth and velocity. At  
 529 depths deeper than 400 m, velocities are fairly constant. The two differing relationships

530 between 150 and 350 m represent velocities from different sides of the glacier. (D)  
531 Relationship between velocity and distance from the lateral margins. The positive correlation  
532 demonstrates the importance of the resistance provided by the fjord walls although depth also  
533 increases with distance from the fjord walls so can also explain this relationship.



535 **Figure 6.** (A) Distribution and patterns of crevasses on Store Glacier. Dry crevasses which  
536 are large structural features are shown in orange. Narrower crevasses that are observed in the  
537 orthorectified images but whose 3D geometry is not constructed are shown in black. The  
538 areas of water-filled crevasses are shown in blue and occur almost exclusively in zone 4. The  
539 regions of the terminus that are discussed are designated by the dotted red lines are referred to  
540 be the black numbers. Transects 1 and 2 shown in inset demonstrate how crevasses advected  
541 downstream between 1 and 2 July. In T1, a series of calving events occurred which are  
542 discussed as ‘calving event A’. In T2, the calving front advanced 16 m. (B) Cartoon of the  
543 terminus of Store Glacier with ellipsoids proportional to the average length, width and  
544 orientation of crevasses shown in (A) for the respective zones. The colour of the ellipsoids  
545 represents the proportion of crevasses that are water-filled in each zone where WF refers to  
546 water-filled in the legend. The italicized numbers denote the density of crevasses per  $10\text{ m}^2$  in  
547 each zone. Arrows illustrate inferred direction of principal strain.

548

549

550

551

552

553

554

555

556

557 *Acknowledgements.* We thank Matt Nolan, Doug Benn and Mauri Pelto for their thorough and  
558 insightful reviews, and Anders Damsgaard for his short comments: all of which greatly improved the  
559 manuscript. Funding for the fieldwork was made possible by the UK Natural Environmental Research  
560 Council (NERC) Grant NE/K005871/1 (Subglacial Access and Fast Ice Research Experiment  
561 (SAFIRE): Resolving the Basal Control on Ice Flow and Calving in Greenland). NERC also funded  
562 The Cryosphere page charges. J.C.R is funded by an Aberystwyth University Doctoral Career  
563 Development Scholarship (DCDS). We are also indebted to the crew of S/V Gambo who worked  
564 tirelessly to provide logistical support, and to the Uummannaq Polar Institute and Children's Home  
565 who provided accommodation in Uummannaq.

566

567

568

569

570

571

572

573

574

575

576

577

578 **References**

579 AgiSoft LLC (2013). AgiSoft PhotoScan. <http://www.agisoft.ru/products/photoscan/> (date of  
580 access: 14 February 2014).

581 Ahlstrøm, A. P., Andersen, S. B., Andersen, M. L., Machguth, H., Nick, F. M., Joughin, I.,  
582 Reijmer, C. H., van de Wal, R. S. W., Merryman Boncori, J. P., Box, J. E., Citterio, M., van  
583 As, D., Fausto, R. S., and Hubbard, A.: Seasonal velocities of eight major marine-terminating  
584 outlet glaciers of the Greenland ice sheet from continuous in situ GPS instruments, *Earth*  
585 *Syst. Sci. Data*, 5, 277-287, doi:10.5194/essd-5-277-2013, 2013.

586 Ahn, Y. and J. E. Box.: Glacier velocities from time-lapse photos: technique development  
587 and first results from the Extreme Ice Survey (EIS) in Greenland, *Journal of Glaciology*, 56,  
588 723–734, doi:10.3189/002214310793146313, 2010.

589 Benn, D. I., Warren, C. R., and Mottram, R. H.: Calving processes and the dynamics of  
590 calving glaciers, *Earth-Science Reviews*, 82, 143-179, doi:10.1016/j.earscirev.2007.02.002,  
591 2007.

592 Benn, D. I., and Evans, D. J. A.: *Glaciers and glaciation*. London: Hodder Education, 2010.

593 Box, J. E., and Decker, D. T.: Greenland marine-terminating glacier area changes: 2000-  
594 2010, *Annals of Glaciology*, 52, 91-98, 2011.

595 Carr, J.R., Vieli, A., and Stokes, C. R.: Climatic, oceanic and topographic controls on marine-  
596 terminating outlet glacier behavior in north-west Greenland at seasonal to interannual  
597 timescales, *Journal of Geophysical Research*, 118, 1210-1226, 2013.

598 d'Oleire-Oltmanns, S., Marzloff, I., Peter, K. D., and Ries, J. B.: Unmanned Aerial Vehicle  
599 (UAV) for monitoring soil erosion in Morocco, *Remote Sensing*, 4, 3390–3416, 2012.



600 Enderlin, E. M., and Howat, I. M.: Submarine melt rate estimates for floating termini of  
601 Greenland outlet glaciers (2000-2010), *Journal of Glaciology*, 59, 67-75,  
602 doi:10.3189/2013jog12j049, 2013.

603 Fitzpatrick, A. A. W., Hubbard, A. L., Box, J. E., Quincey, D. J., van As, D.,  
604 Mikkelsen, A. P. B., Doyle, S. H., Dow, C. F., Hasholt, B., and Jones, G. A.: A decade  
605 (2002–2012) of supraglacial lake volume estimates across Russell Glacier, West Greenland,  
606 *The Cryosphere*, 8, 107-121, doi:10.5194/tc-8-107-2014, 2014.

607 Hambrey, M. J., and Lawson, W.: Structural styles and deformation fields in glaciers: A  
608 review, *Deformation of Glacial Materials*, 176, 59-83, doi:10.1144/Gsl.Sp.2000.176.01.06,  
609 2000.

610 Hock, R.: Glacier melt: a review on processes and their modelling. *Progr. Phys. Geogr.*,  
611 29(3), 362–391, 2005.

612 Holland, D. M., Thomas, R. H., De Young, B., Ribergaard, M. H., and Lyberth, B.:  
613 Acceleration of Jakobshavn Isbrae triggered by warm subsurface ocean waters, *Nature*  
614 *Geoscience*, 1, 659-664, doi:10.1038/Ngeo316, 2008.

615 Howat, I. M., Joughin, I., and Scambos, T. A.: Rapid changes in ice discharge from  
616 Greenland outlet glaciers, *Science*, 315, 1559-1561, doi: 10.1126/science.1138478, 2007.

617 Howat, I. M., Box, J. E., Ahn, Y., Herrington, A., and McFadden, E. M.: Seasonal variability  
618 in the dynamics of marine-terminating outlet glaciers in Greenland, *Journal of Glaciology*,  
619 56, 601-613, 2010.

620 Howat, I. M., Negrete, A., and Smith, B. E.: The Greenland Ice Mapping Project (GIMP)  
621 land classification and surface elevation data sets, *The Cryosphere*, 8, 1509-1518,  
622 doi:10.5194/tc-8-1509-2014, 2014.

623 Hubbard, A.: The Times Atlas and actual Greenland ice loss, *Geology Today*, 27, 214-217,  
624 2011.

625 Hugenholtz, C. H., Levin, N., Barchyn, T. E., and Baddock, M. C.: Remote sensing and  
626 spatial analysis of aeolian sand dunes: A review and outlook, *Earth-Science Reviews*, 111,  
627 319-334, doi:10.1016/j.earscirev.2011.11.006, 2012.

628 Hugenholtz, C. H., Whitehead, K., Brown, O. W., Barchyn, T. E., Moorman, B. J., LeClair,  
629 A., Riddell, K., and Hamilton, T.: Geomorphological mapping with a small unmanned  
630 aircraft system (sUAS): Feature detection and accuracy assessment of a photogrammetrically-  
631 derived digital terrain model, *Geomorphology*, 194, 16-24,  
632 doi:10.1016/j.geomorph.2013.03.023, 2013.

633 Joughin, I., Das, S. B., King, M. A., Smith, B. E., Howat, I. M., and Moon, T.: Seasonal  
634 speedup along the western flank of the Greenland ice sheet, *Science*, 320, 781-783,  
635 doi:10.1126/science.1153288, 2008.

636 Joughin, I., Smith, B. E., Howat, I. M., Floricioiu, D., Alley, R. B., Truffer, M., and  
637 Fahnestock, M.: Seasonal to decadal scale variations in the surface velocity of Jakobshavn  
638 Isbrae, Greenland: Observation and model-based analysis, *Journal of Geophysical Research-  
639 Earth Surface*, 117, doi:10.1029/2011jf002110, 2012.

640 Jung, J., Box, J. E., Balog, J. D., Ahn, Y., Decker, D. T., Hawbecker, P.: Greenland glacier  
641 calving rates from Extreme Ice Survey (EIS) time lapse photogrammetry. C23B-0628,  
642 American Geophysical Union, San Francisco, 2010.

643 Kargel, J. S., Ahlstrøm, A. P., Alley, R. B., Bamber, J. L., Benham, T. J., Box, J. E., Chen,  
644 C., Christoffersen, P., Citterio, M., Cogley, J. G., Jiskoot, H., Leonard, G. J., Morin, P.,  
645 Scambos, T., Sheldon, T., and Willis, I. 2012.: Brief communication. Greenland's shrinking

646 ice cover: "fast times" but not that fast, *The Cryosphere*, 6, 533-537, doi:10.5194/tc-6-533-  
647 2012, 2012.

648 Luckman, A., Murray, T., de Lange, R., and Hanna, E.: Rapid and synchronous ice-dynamic  
649 changes in East Greenland, *Geophysical Research Letters*, 33, doi 10.1059/2005gl025048,  
650 2006.

651 Moon, T., and Joughin, I.: Changes in ice front position on Greenland's outlet glaciers from  
652 1992 to 2007, *Journal of Geophysical Research-Earth Surface*, 113,  
653 doi:10.1029/2007jf000927, 2008.

654 Mottram, R. H., and Benn, D. I.: Testing crevasse-depth models: A field study at  
655 Breioamerkurjokull, Iceland, *Journal of Glaciology*, 55, 746-752,  
656 doi:10.3189/002214309789470905, 2009.

657 Schild, K. M., and Hamilton, G. S.: Seasonal variations of outlet glacier terminus position in  
658 Greenland, *Journal of Glaciology*, 59, 759-770, doi:10.3189/2013jog12j238, 2013.

659 Ullman, S.: The interpretation of structure from motion, *Proceedings of the Royal Society of*  
660 *London B203*, 405–426, 1979.

661 Verhoeven, G.: Taking computer vision aloft – archaeological three-dimensional  
662 reconstructions from aerial photographs with Photoscan, *Archaeological Prospection*, 18, 67–  
663 73, 2011.

664 Vieli, A., Funk, M., and Blatter, H.: Tidewater glaciers: Frontal flow acceleration and basal  
665 sliding, *Annals of Glaciology*, 31, 2000, 31, 217-221, doi:10.3189/172756400781820417,  
666 2000.

667 Xu, Y., Rignot, E., Fenty, I., Menemenlis, D., and Flexas, M. M.: Subaqueous melting of  
668 Store Glacier, West Greenland from three-dimensional, high-resolution numerical modeling

669 and ocean observations, *Geophysical Research Letters*, 40, 4648-4653,  
670 doi:10.1002/Grl.50825, 2013.

671 Walter, J. I., Box, J. E., Tulaczyk, S., Brodsky, E. E., Howat, I. M., Ahn, Y., and Brown, A.:  
672 Oceanic mechanical forcing of a marine-terminating Greenland glacier, *Annals of*  
673 *Glaciology*, 53, 181-192, doi:10.3189/2012aog60a083, 2012.

674 Weertman, J.: Can a water-filled crevasse reach the bottom surface of a glacier?, *IAHS Publ.*,  
675 95, 139–145, 1973.

676 Whitehead, K., Moorman, B. J., and Hugenholtz, C. H.: Brief communication: Low-cost, on-  
677 demand aerial photogrammetry for glaciological measurement, *Cryosphere*, 7, 1879-1884,  
678 doi:10.5194/tc-7-1879-2013, 2013.

679 Weidick, A.: Greenland, with a section on Landsat images of Greenland, in, *Satellite image*  
680 *atlas of glaciers of the world*, Williams, R. S., and Ferrigno, J.G. eds, US Geological Survey,  
681 Washington, DC, C1–C105 (USGS Professional Paper 1386-C), 1995.